Journal of Materials Chemistry A

ROYAL SOCIETY OF CHEMISTRY

PAPER

View Article Online
View Journal | View Issue

Cite this: J. Mater. Chem. A, 2024, 12, 11004

Live-tracking of beef freshness by sub-ppb level ammonia detection using WS_2/rGO nanoflakes incorporating edge site-enriched acidic sulfur†

Sonam Sonwal,[a] Kugalur Shanmugam Ranjith,[b] Soobin Han,[a] Young-Kyu Han,[b]* Mi-Hwa Oh*[c] and Yun Suk Huh[a]*

Received 18th December 2023
Accepted 25th March 2024

DOI: 10.1039/d3ta07831k

rsc.li/materials-a

Highly accurate, easily accessible room temperature wireless gas-sensing technology can be utilized to monitor food freshness in real time to prevent food fraud and spoiled food consumption, thus safeguarding humans from diseases. In this work, we coupled a high-sensitivity ammonia gas sensor with interface transmitter/gateway Bluetooth technology to produce a wireless communication system for live tracking beef freshness. Herein, we propose a chemiresistive gas sensor containing hydrothermally produced sulfur-rich WS_2/rGO hierarchical nanoflakes for gas sensing at RT. The as-developed nanohybrid was subjected to various physicochemical techniques, including XRD analysis, HR-SEM, FE-TEM, FTIR spectroscopy, Raman spectroscopy, and XPS. The sensitivity of the sulfur-rich WS_2/rGO nanohybrid towards NH_3 was twice as high as that of pristine sulfur-rich WS_2 with an LOD of 0.5 ppb and a response of 7.5% at RT. The NH_3-sensing mechanism was attributed to a negative charge donated by NH_3 on the positively charged sulfur-rich WS_2/rGO composite, which enabled it to interact with certain functional groups (SO_3H, –OH, and H_2O) and enhanced the resistance of the material. In addition, the composite had a 3.7-fold greater response to NH_3 than other VOCs and great stability after 25 cycles. Moreover, the practical application potential was also evaluated for beef freshness monitoring. This technology can be expanded to rapidly tune gas-sensing active materials *via* nanoengineering for various applications in wireless gas sensors, such as air-quality, automobile-exhaust, food-deterioration, and gas-leak monitoring.

1. Introduction

Food spoilage and fraud during transportation are alarming logistical issues in the global supply chain.[1–5] Contaminated or spoiled food items can have deadly consequences, including food poisoning, long-term diarrhea, high fever, loss of eyesight or speech, severe dehydration, and hematuria.[6–11] In this regard, wireless and real-time monitoring integrated gas-sensing technology has the potential to revolutionize this sector by enabling the real-time tracking of food spoilage.[1,6,12,13] The Internet of Things (IoT) and artificial intelligence (AI) have emerged as key future players by enabling wireless connectivity using built-in hardware and digital/cloud connectivity.[14–17] Food monitoring utilizes a variety of wireless electronic technologies, including Bluetooth low energy (BLE) transmitters, radio frequency identification (RFID), near-field communication (NFC), and wireless sensor networks (WSNs).[18–27] The best real-time detection is ensured by BLE systems owing to their low power consumption and low price.

Recent developments in the chemical and physical characteristics of low-dimensional semiconductor nanoparticles have been adopted for the development of RT gas sensors. The development of semiconductor-based gas sensors with ultra-low power consumption in RT environments is fueling the need to introduce gas sensors. In this regard, advanced, solution-based synthetic processes can considerably reduce manufacturing costs and facilitate the industrial-scale production of nanomaterials.[28–32]

Semiconductor-based gas sensors are highly sensitive, economically viable, and viewed as the future of gas sensing. Gas sensors come in a variety of forms, such as chemiresistive, optical, electrochemical, and field effect transistor (FET) types and are easily manufactured, have great sensing performance, are cost-effective, and consume less power. Chemiresistive-type gas sensors are the most widely used sensor type. Metal-oxide-semiconductor (MOS) sensors of this type exhibit enhanced sensitivity for target gases at elevated temperatures (>200 °C) but

[a]NanoBio High-Tech Materials Research Center, Department of Biological Engineering, Inha University, Incheon 22212, Republic of Korea. E-mail: yunsuk.huh@inha.ac.kr
[b]Department of Energy and Material Engineering, Dongguk University-Seoul, Seoul 04620, Republic of Korea. E-mail: ykenergy@dongguk.edu
[c]National Institute of Animal Science, Rural Development Administration, Wanju 55365, Republic of Korea. E-mail: moh@korea.kr

† Electronic supplementary information (ESI) available. See DOI: https://doi.org/10.1039/d3ta07831k

have high power consumption.[28,33,34] Moreover, MOS sensors lack selectivity and cannot be used to detect low gas concentrations. Therefore, research efforts have focused on the surfaces and interface properties to develop RT-compatible gas sensors with outstanding sensing performances and low detection limits.[35–38] The creation of next-generation gas sensors for sensing at RT depends heavily on the properties of two-dimensional (2D) semiconductor nanomaterials,[39–41] which are usually chosen because of their greater specific surface areas and higher surface activities.[28,40] Recent additions to the 2D material family include transition metal dichalcogenides (TMDs), black phosphorus, MXenes, and layered metal oxides, with TMDs attracting particular interest as a class of gas-sensitive materials for NH_3, NO_2, and H_2 detection at RT. Actually, the superior characteristics of 2D TMDs, which include high surface-to-volume ratios and good conductivities in air, make them highly sensitive to absorbed gases and near perfect for RT gas detection. Numerous studies have been conducted on TMDs for gas-sensing applications, and a variety of techniques have been used to enhance their sensing capabilities.[28,41–43] However, improvements are still needed, including faster response/recovery rates at RT, long-term stability, ultra-low detection limits, and the selectivity of 2D gas sensors to enable their usage in indoor or outdoor gaseous environments.[28]

Reduced graphene oxide (rGO)-based chemiresistive gas sensors have attracted much attention since graphene was first discovered.[44] The majority of the literature emphasizes that rGO is selective for ammonia gas.[44–46] A low detection limit, an enhanced higher response, better selectivity, and the ability to combine the desirable properties of various nanoscale building blocks to improve materials' chemical and electronic properties have all been found to be effectively improved by the modification of rGO with metal oxide/organic ligands. Numerous studies have shown that hybrid structures of graphene and nanoparticles can work synergistically to provide a variety of special physicochemical features that are favorable and desirable for sensing applications.[47–49] Numerous metal or metal oxide/rGO nanocomposites, such as Pt-SnO_2/rGO, SnO_2/rGO, Co_3O_4/rGO, ZnO/rGO, Pd-rGO, rGO/Cu_2O, rGO-SO_3H^-, rGO-SO_3H^-/Ag, rGO/NiO, rGO/Ag/Au, and MoO_3/rGO, have been produced and utilized for chemical gas sensors.[47,48] Compared to the comparable pure systems, all these hybrids of rGO-MOx/organic ligands show substantially better response/recovery characteristics and increased sensitivity at ambient temperature. As a p-type rGO semiconductor with highly attractive features, such as rich specific active sites and a strong adsorption ability to gas molecules, such as nitrogen dioxide and ammonia, rGO plays a critical role in the gas-sensing processes of hybrid sensing composites.[44,45,47,48,50–54]

Fresh meat is an excellent source of the nutrients required to meet metabolic demands, but consumers are increasingly interested in meat freshness, quality, and safety in addition to the nutritional content.[55–58] Since ancient times, meat-borne illnesses have been a major public health concern. During the initial stages of meat decay, volatile organic compounds (VOCs) are produced at ppm to ppb levels and are not detected by the human olfactory system, which can lead to the consumption of spoiled meat and potential illness, such as food poisoning, long-term diarrhea, high fever, loss of eyesight or speech, severe dehydration, bloody urine, nausea, vomiting, and stomach pain. According to World Health Organization (WHO) estimates, eating contaminated food causes 600 million illnesses, affecting around 1 in 10 persons, and ~420 000 fatalities per annum.[8,59]

Nonetheless, the gases released during food decomposition provide a reliable biomarker of meat freshness. For instance, protein breakdown results in the release of ammonia (NH_3), hydrogen sulfide, ethanol, aldehydes, ketones, organic acids, and tiny amounts of total volatile basic nitrogen (TVBN) compounds, like NH_3, DMA, and TMA, and biogenic amines (BAs), such as cadaverine, putrescine, spermidine, spermine, phenylethylamine, and histamine. Thus, meat freshness can be quickly detected using nanomaterial-based gas-sensing technology targeting volatile amines at the ppb level.[8,10] WS_2, MoS_2, and SnS_2 have been widely researched for gas sensing. Wang *et al.*[60] used a rGO/WS_2 composite with minimal sulfonate decoration for NH_3 sensing at RT. MoS_2 structurally mimicking reactivated WS_2 nanoflakes was reported by Li *et al.*[61] and exhibited a high sensitivity and excellent selectivity for NH_3 at RT. Gu *et al.*[62] demonstrated that light-enhanced WS_2 microflakes were more sensitive and selective for NH_3. Huo *et al.*[63] reported photoresponsive and gas-sensing FET-type sensor multilayer WS_2 nanoflakes. However, all the sensors described to date have limitations in selectivity, sensitivity, stability, or RT sensing abilities.

Utilizing wireless communication technology is crucial for real-world applications because it enables the use of RT semiconductor gas sensors and supports to address the current challenges of onsite monitoring. Consequently, we developed a cloud-based meat-freshness monitoring system to address the sensitivity, selectivity, and stability shortcomings of the current sensors at temperatures ≤RT. We selected WS_2 as the receptor because of its beneficial characteristics, which include a suitable band structure, phonon-limited electron mobility, and thermal stability. The slow recovery and targeting of low concentration NH_3 at RT was rectified by hybridizing rGO with WS_2 and by altering the oxalic acid concentration in the presence of thiourea. It has been demonstrated that sulfonic acid on nanoflakes surfaces inhibits the formation of acid centers by sulfate groups and improves the adsorption and desorption of ammonia molecules. We opted for a hydrothermal route to prepare sulfur-rich WS_2/rGO and targeted NH_3 as a biomarker to create a gas sensor with general utility for early meat spoilage detection. In addition, we coupled our sensor with a BLE-based cloud communication system to enable real-time meat-freshness monitoring. This was also done to enable the sensor to be applicable for other uses, such as monitoring in factories, chemical plants, and laboratories, for monitoring environmental pollution, waste gas emissions, gas leakage in dangerous situations, and for healthcare diagnosis.[64–76]

2. Experimental procedure

2.1. Materials and methods

Ammonium tungsten oxide hydrate ($(NH_4)_{10}W_{12}O_{41}\cdot xH_2O$), thiourea ($CH_4N_2S$), oxalic acid ($C_2H_2O_4$), graphene oxide (GO), ethanol (C_2H_5OH), methanol (CH_3OH), acetone (C_3H_6O),

benzene (C_6H_6), ethyl acetate ($C_4H_8O_2$), hexane (C_6H_{14}), 2-propanol (C_3H_8O), toluene (C_7H_8), styrene (C_8H_8), dimethylacetamide (DMA, C_4H_9NO), and trimethylamine (TMA, C_3H_9N) were purchased from Sigma-Aldrich and used as received without further purification. Nitrogen gas (N_2), ammonia gas (NH_3), ethanol (C_2H_5OH), methane (CH_3), and nitrogen dioxide gas (NO_2) were purchased from GRAND gas brand with a high purity of 99.999%. Other consumables included deionized water (DW), Teflon beakers/liners, hydrothermal vessels, a muffle furnace, a freeze dryer, parallel gold electrodes printed over a silicon wafer, a bubbler, and Keithley sensing setup (GMC1200).

2.2. Preparation of pristine sulfur-rich WS_2

Tungsten and sulfur sources were used to prepare 2D sulfur-rich WS_2. Briefly, 0.7 g of $(NH_4)_{10}W_{12}O_{41}\cdot xH_2O$ and 0.7 g of CH_4N_2S were dissolved in 40 ml of DW and stirred for 30 min. To study the acid environmental effect, three different amounts of $C_2H_2O_4$ (0.45, 0.9, or 1.35 g) were added to three replicate of the above-mentioned solutions separately and stirred for 30 min. Higher $C_2H_2O_4$ contents facilitate the formation of sulfonic acid in the presence of CH_4N_2S and promote the synthesis of a sulfur-rich WS_2 nanostructure. All three replicate solutions with different concentration of $C_2H_2O_4$ were transferred to three separate 40 ml Teflon-lined autoclaves, heated at 200 °C for 20 h, and cooled to RT, and the resulting black precipitates were washed with ethanol three times and then with DW three times using a centrifuge at 7000 rpm for 5 min. The precipitates were collected, frozen, and freeze-dried. The black, lump-free, powder samples were collected and stored in airtight vials until required.

2.3. Preparation of sulfur-rich WS_2/rGO

The composition of sulfur-rich WS_2/rGO was finalized by checking the sensing ability of the sulfur-rich WS_2, and the best-performing material's composition was further modified, and synthesized by adding GO. Four different weight percentages of GO were prepared (10%, 20%, 30%, and 40%) in 40 ml DW and sonicated for 20 min. All the contents of the best-performing sulfur-rich WS_2 (0.7 g of $(NH_4)_{10}W_{12}O_{41}\cdot xH_2O$) and 0.7 g of CH_4N_2S and 1.35 g $C_2H_2O_4$ were added to the GO solution and stirred for 30 min. This was followed by hydrothermal treatment using the same parameters used to produce sulfur-rich WS_2 (Fig. 1a). Finally, the sulfur-rich WS_2/rGO composite was collected after washing and freeze-drying.

2.4. Fabrication of the gas sensor

A solution of 3 mg of the sulfur-rich WS_2/rGO composite was prepared in 500 μl of ethanol in an Eppendorf tube, sonicated for 1 h, and then centrifuged at 7000 rpm for 5 min to achieve a paste-like consistency. The supernatant was then discarded, and the precipitate was collected. Next, 1 μl of the thick sulfur-rich WS_2/rGO paste was drop-cast over the interjection space of a parallel gold electrode and then vacuum dried for 1 h at 60 °C (Fig. 1b). Micrometer-sized silicon wafer-based gold parallel electrodes were used to drop-cast the sensing material. The gas-sensing micro-space system with a 0.3 mm gap was made by stacking gold electrodes using a sputtering method. Sulfur-rich WS_2/rGO covered and functionalized the exposed gold surface, and a chemiresistive bridge was formed across the sulfur-rich WS_2/rGO-coated micro-space when the device was exposed to NH_3.

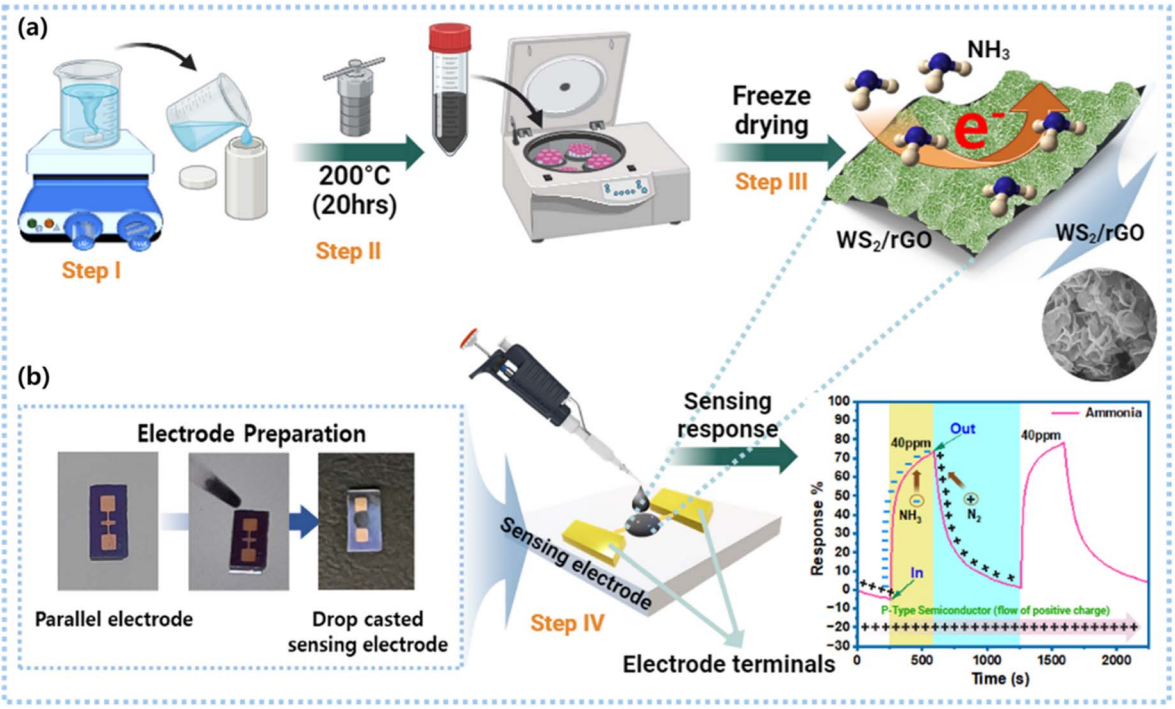

Fig. 1 Schematic of the synthesis of the sulfur-rich WS_2/rGO composite and fabrication of the sensing electrode: (a) hydrothermal synthesis of sulfur-rich WS_2/rGO; (b) electrode preparation by drop-casting the sulfur-rich WS_2/rGO composite over the gold electrode interjunction space.

2.5. Characterizations

High-resolution scanning electron microscopy (HRSEM, Hitachi S-520, operated at 18 kV) and field emission scanning electron microscopy (FETEM, JEM-2100F, JEOL Japan, working at 20 kV) were used to study the morphology of the sulfur-rich S_2/rGO composite. Selected area electron diffraction (SAED) patterns, fast Fourier transform (FFT) images, and high-resolution TEM (HRTEM) images were obtained using a field emission electron microscope (JEOL-JEM-2100F) operating at 20 kV. TEM samples were produced by drop-casting an ethanolic dispersion onto a carbon-covered Cu grid. Fourier transform infrared spectroscopy (Bruker FT/IR-6600 scanning in the 400–4000 cm^{-1} range) was used to identify the surface functionality and types of bonding. An X-ray photoelectron spectrometry system (XPS) (Thermo Scientific spectrometer, Al K radiation (1486.6 eV)) equipped with a multi-channel detector was used to analyze the surface elemental compositions and structural properties of the sulfur-rich WS_2/rGO composite. An X-ray diffractometer and CuK radiation of 1.54056 Å (Bruker D2 phaser X-ray diffractometer) were used to obtain X-ray diffraction (XRD) patterns. A laser Raman spectrometer (Raman, FEX, NOST, Republic of Korea) was used to analyze the WS_2/rGO composites at a wavelength of 532 nm.

2.6. Gas-sensing measurements *via* a Keithley meter

The *R–V* characteristics of the sensing devices were measured in the range of 0.5–2.5 V at RT using a Keithley source meter [Keithley (GMC1200)] controlled by NEXTRON software. All the parameters, such as temperature, time, voltage, current, and gas flow rate, were inputted into the software, which controlled the power supplier and voltage supply. The Keithley meter also recorded and displayed the resistive responses of the sensor. MFCs were used to maintain the gas flow rates and pressures. Simultaneously, relative humidity (RH) was monitored using a RH sensor within the gas-sensing chamber. All the experiments were performed at a constant 70% RH to simulate the real-time internal environment of a packed meat box. A 250 cm^3 stainless steel gas-sensing test equipment with a hot plate probe station, thermocouple, and systematic gas inlet–outlet was used to test the characteristics and responses of the gas sensors. The target analyte gas was diluted with the carrier gas N_2 at different flow rates (sccm) to vary the gas concentrations. The final concentration of gas was calculated using eqn (1):

$$C_2(\text{ppm}) = \frac{C_1 \times V_1}{V_2} \quad (1)$$

where C_1 is the gas concentration (ppm), V_1 is the flow rate of the analyte gas, V_2 is the total flow of the diluted gas (analyte and N_2), and C_2 is the final gas concentration. The sensor response % (S%) was calculated using eqn (2), where R_{gas} is the electric resistance of sulfur-rich WS_2/rGO in an ammonia atmosphere and R_{N2} is the electric resistance in a nitrogen atmosphere.

$$S\% = \frac{R_{gas} - R_{N_2}}{R_{N_2}} \times 100\% \quad (2)$$

The response and recovery time of the sensor were calculated by eqn (3) and (4).

$$\text{Response time} = R_N + 90\%\ \Delta R \quad (3)$$

$$\text{Response time} = R_g + 90\%\ \Delta R \quad (4)$$

$$\Delta R = |R_g - R_N| \quad (5)$$

where ΔR is the resistance difference between R_g and R_N.

2.7. Real-time beef freshness monitoring using the BLE-based smart meat distribution box

Fresh beef was used as a model sample for the real-time experiments. Acquired and uploaded data were recorded in real-time in terms of the current magnitude at 400 mV and 10 mA parameters using the BLE-based cloud-communicating device coupled with a transmitter connected to a two-electrode system. The smart box was hand-fabricated and assembled in the laboratory by coupling the BLE device and sensing electrodes. Beef freshness was monitored daily from day one after setting all the sensing parameters. Recorded data were collected as current magnitudes and converted into resistance to enable comparisons with the Keithley meter and smart box response data.

3. Result and discussion

Straightforward hydrothermal approaches can be used to construct hybrid nanostructures of 2D materials. These hybrid nanostructures are composed of two 2D materials and contain many sharp edges and significant numbers of nano-protrusions. Furthermore, hybrid nanostructures ought to have better gas-response characteristics because of their morphological, surface area, and active site modifications. Here, we compared the dynamic gas responses of sulfur-rich WS_2/rGO and sulfur-rich WS_2 nanoflakes.

3.1. Structural, surface, and morphological characterizations

Sulfur-rich WS_2/rGO was synthesized using a hydrothermal process in the presence of a sulfur source in a highly acidic environment. Fig. 10 provides a schematic of the functional groups on the surfaces and edges of graphene oxide as determined by the instrumental investigations performed.

The crystalline structures of the sulfur-rich WS_2 and sulfur-rich WS_2/rGO were determined by X-ray diffraction (Fig. 2a–c). The JCPDS card of hexagonal WS_2 (84-1398) contained peaks matching the XRD peaks of sulfur-rich WS_2 and sulfur-rich WS_2/rGO.[77,78] The XRD patterns of the sulfur-rich WS_2/rGO composite, sulfur-rich WS_2, and rGO are displayed in Fig. 2a–c. In order to quantify the presence of rGO in the composites, the *y*-axis of the XRD spectrum of all samples is provided in the log scale. All prominent diffraction peaks (at $2\theta = 13.52°$, 33.81°, 27.88°, and 59.28°) were directly attributable to 2H-WS_2, which confirmed the excellent purity of the sulfur-rich WS_2 produced (Fig. 2b). Every reflection peak was indexed to the hexagonal

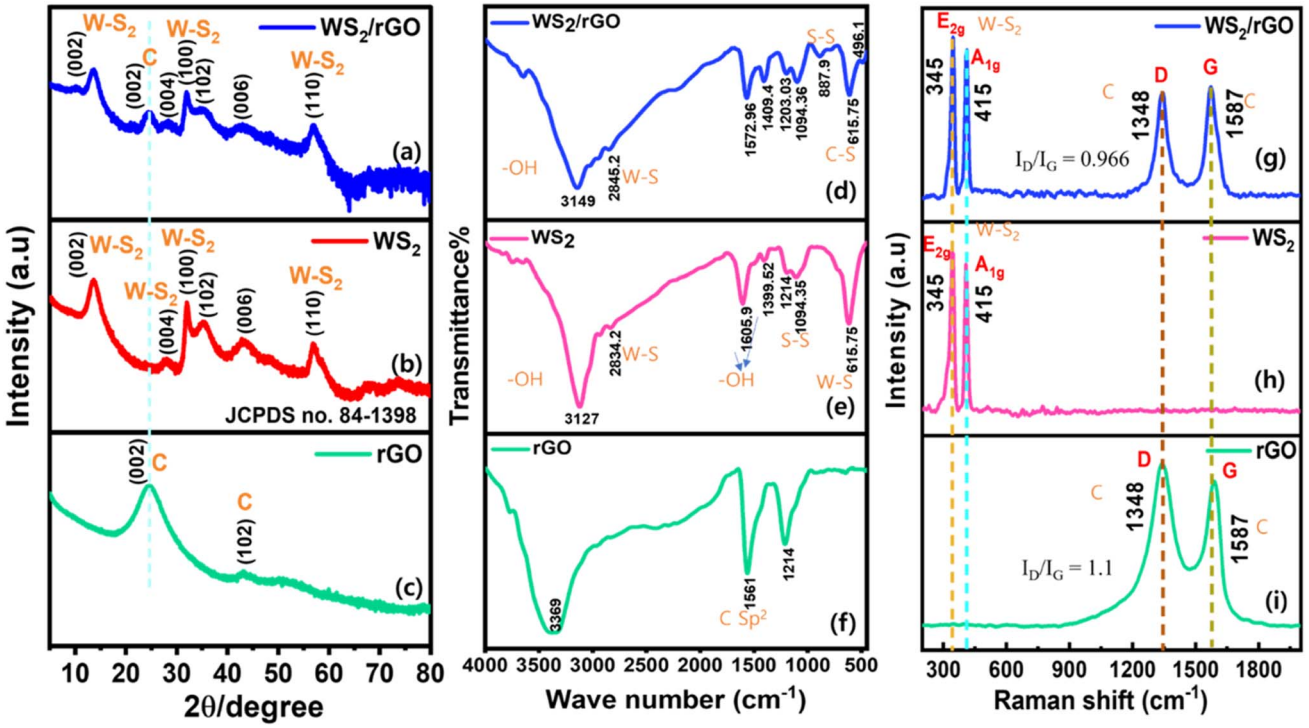

Fig. 2 Structural and molecular analysis of the sulfur-rich WS_2/rGO composite, sulfur-rich WS_2, and rGO: (a–c) XRD of the composite sulfur-rich WS_2/rGO, sulfur-rich WS_2, and rGO; (d–f) FT-IR of the composite, sulfur-rich WS_2, and rGO; (g–i) Raman spectra of the composite, sulfur-rich WS_2, and rGO.

WS_2 phase and was consistent with the standard JCPDS card no. 84-1398. Furthermore, the existence of (002), (100), (004), and (110) plane reflections attested to the existence of a few-layered arrangement in the sulfur-rich WS_2. The XRD data of the WS_2 sheets showed that the direction of sheet growth was along the (002) direction. The XRD pattern of the WS_2/rGO composite showed a broad (002) peak and more intense (100, 102, 006, and 110) peaks compared to the WS_2 sheets (Fig. 2c). The broadness of the (002) peak indicated both the smaller size and fewer layers of the WS_2 sheets compared to the pristine WS_2 nanomaterial.[78] In addition, the peak present at 24.54° evidenced the presence of (002) planes of a carbon-related peak, representing the presence of rGO in the composite (Fig. 2a). The diffraction peaks of sulfur-rich WS_2/rGO well matched those of sulfur-rich WS_2, but the peak intensities were clearly reduced due to the presence of rGO in the composite and the reduced numbers of incoming and reflected X-ray photons in the presence of rGO.[60,61,79] According to these results, hybridization with rGO did not significantly modify the crystalline structure of sulfur-rich WS_2.

The FT-IR spectra of the sulfur-rich WS_2/rGO composite, sulfur-rich WS_2, and rGO are shown in Fig. 2. The vibrational band at 2834.2 cm^{-1} was ascribed to W–S bending vibrations and the vibrational band at 3127 cm^{-1} to atmospheric –OH. The bands at 1605.9 and 1399.5 cm^{-1} were attributed to the stretching vibrations of hydroxyl groups, while the bands at 1094.1 and 615.8 cm^{-1} were related to S–S and W–S bond vibrations, respectively (Fig. 2e). The bands of the sulfur-rich WS_2/rGO composite at 615.8 and 496.1 cm^{-1} were attributed to C–S and S–S stretching vibrations. With slight repositioning, the majority of the characteristic bands of WS_2 were visible in the spectrum of the sulfur-rich WS_2/rGO composite (Fig. 2d). The band at 615.8 cm^{-1} was attributed to C–S in the composite, while the bands at 2834.2 and 2845.8 cm^{-1} were ascribed to W–S in the sulfur-rich WS_2 and the composite, confirming the composite formation.[80] The intensity of the peak signal at 3369 cm^{-1} diminished after the hydrothermal reduction of GO, while the peak at 1736 cm^{-1} contracted, indicating the decomposition of the carboxyl groups. Rebuilding of the sp^2 carbon network in the composite was confirmed by the strong signal at 1561 cm^{-1} (Fig. 2f).[81] the FT-IR data showed that abundant hydroxyl groups remained after hydrothermal reduction, which was considered the primary cause of the improved response.

The Raman spectra shown in Fig. 2g–i contain labeled peaks that constitute the "fingerprints" of sulfur-rich WS_2/rGO, sulfur-rich WS_2, and rGO, respectively. As demonstrated by the Raman shift of the sulfur-rich WS_2/rGO, sulfur-rich WS_2, and rGO in Fig. 2g–i, the peaks at 345 and 415 cm^{-1} corresponded to the E_{2g} and A_{1g} modes of WS_2, respectively. Sulfur-rich WS_2/rGO and rGO both contained the graphene peaks known as "D" and "G" bands within the range 1000–2000 cm^{-1}. Graphene's E_{2g} mode of carbon atoms is related to the G band, while the D band is related to defects.[60,61] A comparison of the spectra of the sulfur-rich WS_2/rGO and rGO revealed low-position migrations of the D bands, attributed to binding sites between rGO and sulfur-

rich WS_2. We suppose the heterojunction containing nature of the WS_2/rGO composite may explain the observed G band shift compared to rGO. In graphene-based materials, the I_D/I_G ratio (the intensity ratio of the "D" and "G" bands) is inversely proportional to the normal size of sp^2 clusters. Furthermore, the "D" and "G" bands in the Raman spectra of the composite were weaker than those of rGO, which we speculated may have been caused by non-polar groups in the composite. The calculated I_D/I_G ratios of rGO and WS_2/rGO were 1.1 and 0.966, respectively. rGO showed higher defects and a less graphitic nature, which later showed a reversible property in the WS_2/rGO composite. The WS_2/rGO composite had less defects and a higher graphitic nature; thus rGO plays a crucial role in enhancing the sensing properties of the sulfur-rich WS_2/rGO composite. The groups in the composite had large vibratory dipole moments and exhibited modest Raman activity but substantial infrared activity (Fig. 2d–f).

HRSEM and FETEM were used to examine the microstructure and morphology of the as-prepared samples. HRSEM images at various magnifications are shown in Fig. 3a–f. The synthesized sulfur-rich WS_2/rGO composite samples were primarily composed of WS_2 nanoflakes (Fig. 3e). High-magnification SEM (Fig. 3f) revealed details of the microstructure of the nanoflakes and showed that they homogeneously and completely decorated rGO, were loosely layered, and were ~2 nm thick with widths between 100 and 150 nm. Furthermore, the presence of rGO is shown in Fig. S6,† which also shows that the morphology was disrupted by the addition of a high rGO content (10%, 20%, 30%, and 40%) while simultaneously maintaining the homogenous covering of all the rGO particles. Fig. 3a and b show the wrinkled morphology of rGO, which was responsible for the distorted arrangement of nanoflakes and rolling up of the nanoflakes. FETEM images of the samples are shown in Fig. 4a–f. The samples were primarily composed of ultrathin and evenly scattered flakes, as shown by the low-magnification FETEM images in Fig. 3d–e. The morphology observed in the SEM images was consistent with that observed in the FETEM images. In addition, the (002) peak of sulfur-rich WS_2 indicated a crystal interplanar spacing of 0.62 nm (Fig. 4f).[78] Moreover, some sulfur-rich WS_2 nanoflakes were somewhat bent, possibly because these extremely thin two-dimensional substances could be easily rolled into closed structures, which also prevented connections at the nanoflake edges. The ultrathin flake structure is shown in more detail in Fig. 4e. The energy dispersive spectra (Fig. 4i–m) of the sulfur-rich WS_2/rGO revealed a homogenous distribution of C, O, N, W, and S elements, with atomic composition of 49.40%, 12.87%, 2.41%, 10.67%, and 24.65% (inset of Fig. 4g).

XPS was used to classify the molecular phases and oxidation states in the sulfur-rich WS_2/rGO composite. The four core level peaks for W, namely 4f, S 2p, C 1s, and O 1s, are presented in Fig. 5a inset. The observation of less O 1s state in the sulfur-rich WS_2/rGO nanohybrid showed that the hydrothermal procedure effectively reduced GO to rGO. The three core functional peaks at 284.8 eV (C–C), 286.4 eV (C–O), and 289.2 eV (C=O) represent C bonding (Fig. 5a) and depict the C 1s deconvoluted spectrum of the sulfur-rich WS_2/rGO composite.[60] the less intense O-bond signals in the C 1s spectrum of the composite further support its lower O-content. Fig. 5b shows the O 1s information, in which the main peak of O at 531.11 eV implied the existence of oxygen vacancy (Ov) states in the WS_2/rGO composite. In addition, a small peak at 532.65 eV was observed, attributed to the

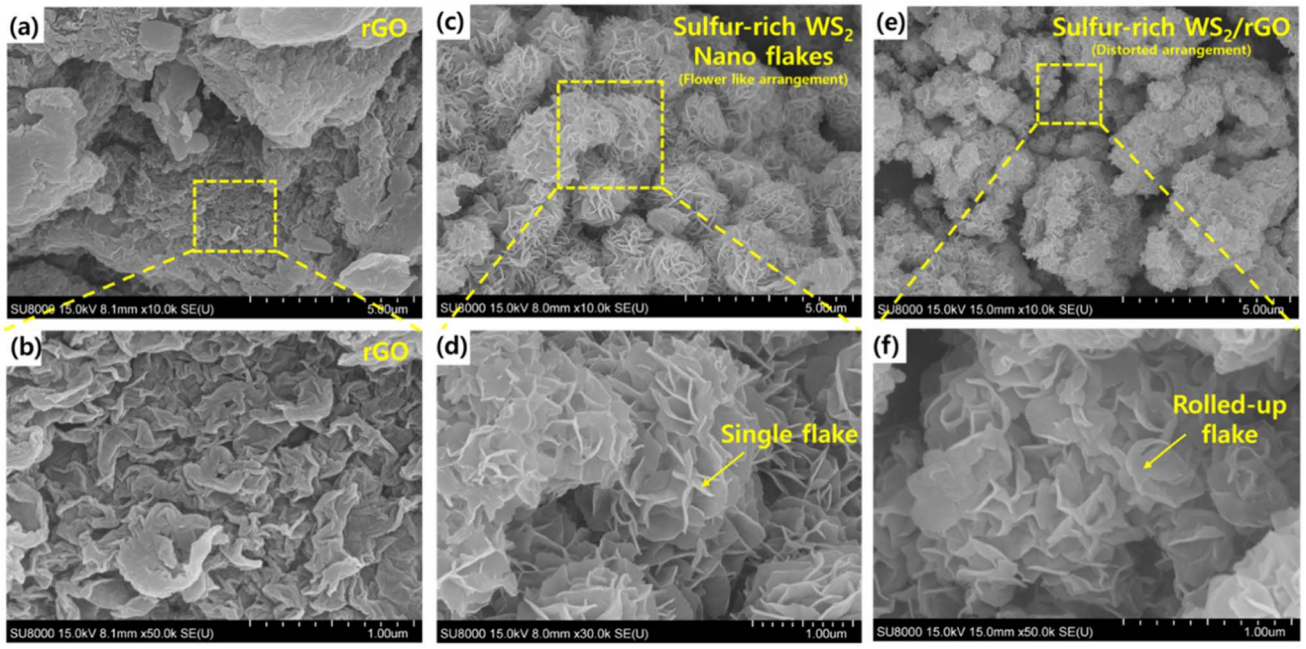

Fig. 3 HRSEM images of rGO, sulfur-rich WS_2, and the sulfur-rich WS_2/rGO composite: (a and b) HRSEM images of rGO at different magnifications; (c and d) showing the flower-like arrangement of pristine sulfur-rich WS_2 nanoflakes at different magnifications; (e and f) showing the distorted arrangement of sulfur-rich WS_2/rGO composite nanoflakes (rolled-up) at different magnifications.

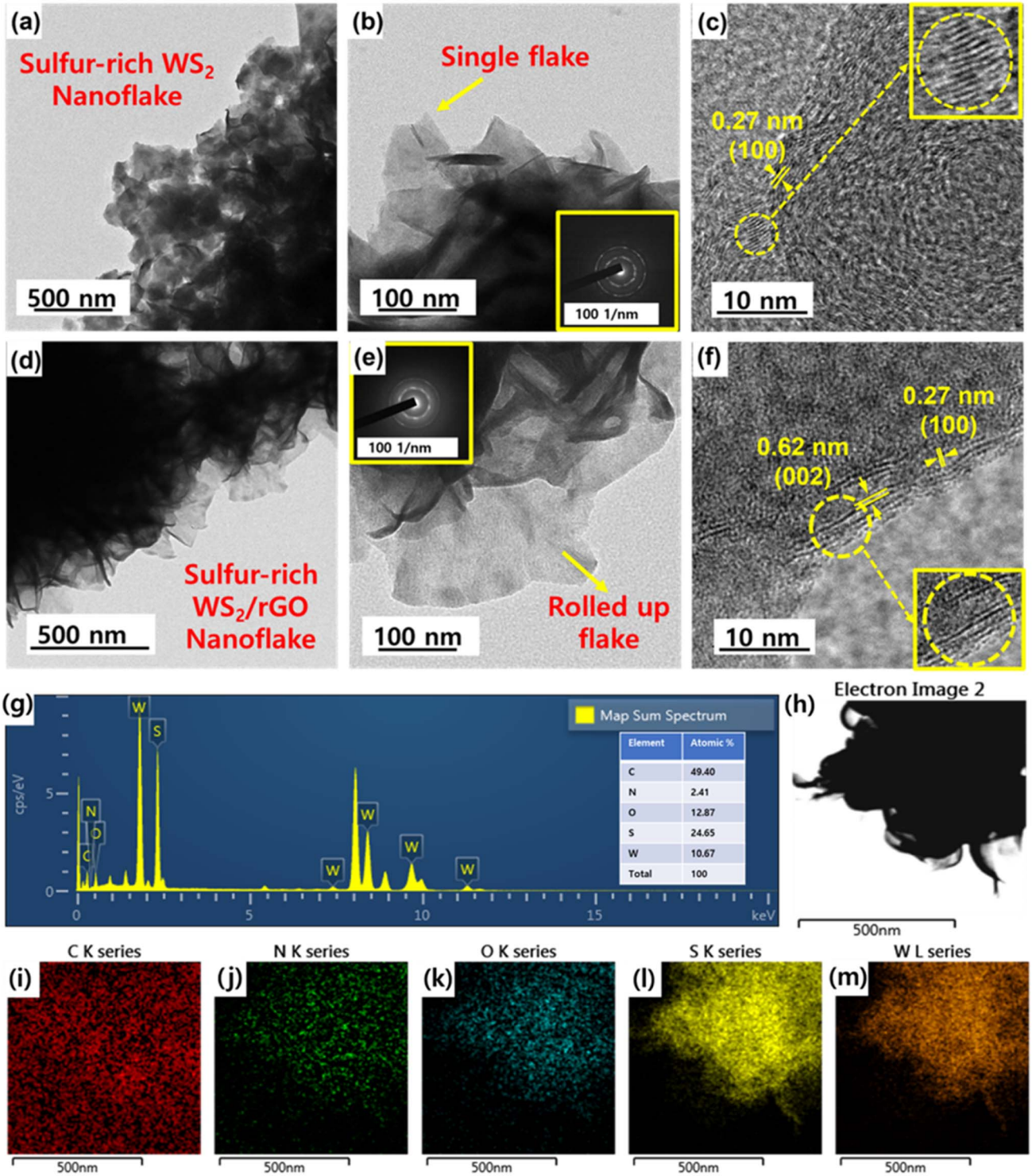

Fig. 4 FETEM images of sulfur-rich WS_2 and the sulfur-rich WS_2/rGO composite: (a–c) nanoflake arrangement of pristine sulfur-rich WS_2 nanoflakes at different magnifications; (d–f) rolled-up flake arrangement of sulfur-rich WS_2/rGO composite nanoflakes at different magnifications. Insets in (b) and (e) show the SAED patterns of sulfur-rich WS_2 and the sulfur-rich WS_2/rGO composite, respectively; (g) EDAX spectra of the sulfur-rich WS_2/rGO composite; (h–m) elemental mapping of the sulfur-rich WS_2/rGO composite.

carboxylic interaction in the WS_2/rGO composite.[82] The binding energies of two satellite shakeup peaks at 32.39 and 34.42 eV (refer to the W 4f spectrum in Fig. 5c) showed W $4f_{7/2}$ and W $4f_{5/2}$ as distinguishing features. Simultaneously, the modest peaks at 36.11 and 38.24 eV were attributed to the W $4f_{7/2}$ and W $5p_{3/2}$ of oxides originating from WO_x with higher binding energies on the surface of the as-prepared sulfur-rich composite.[60,61] According to Fig. 5d, which depicts the spectrum of S 2p, the

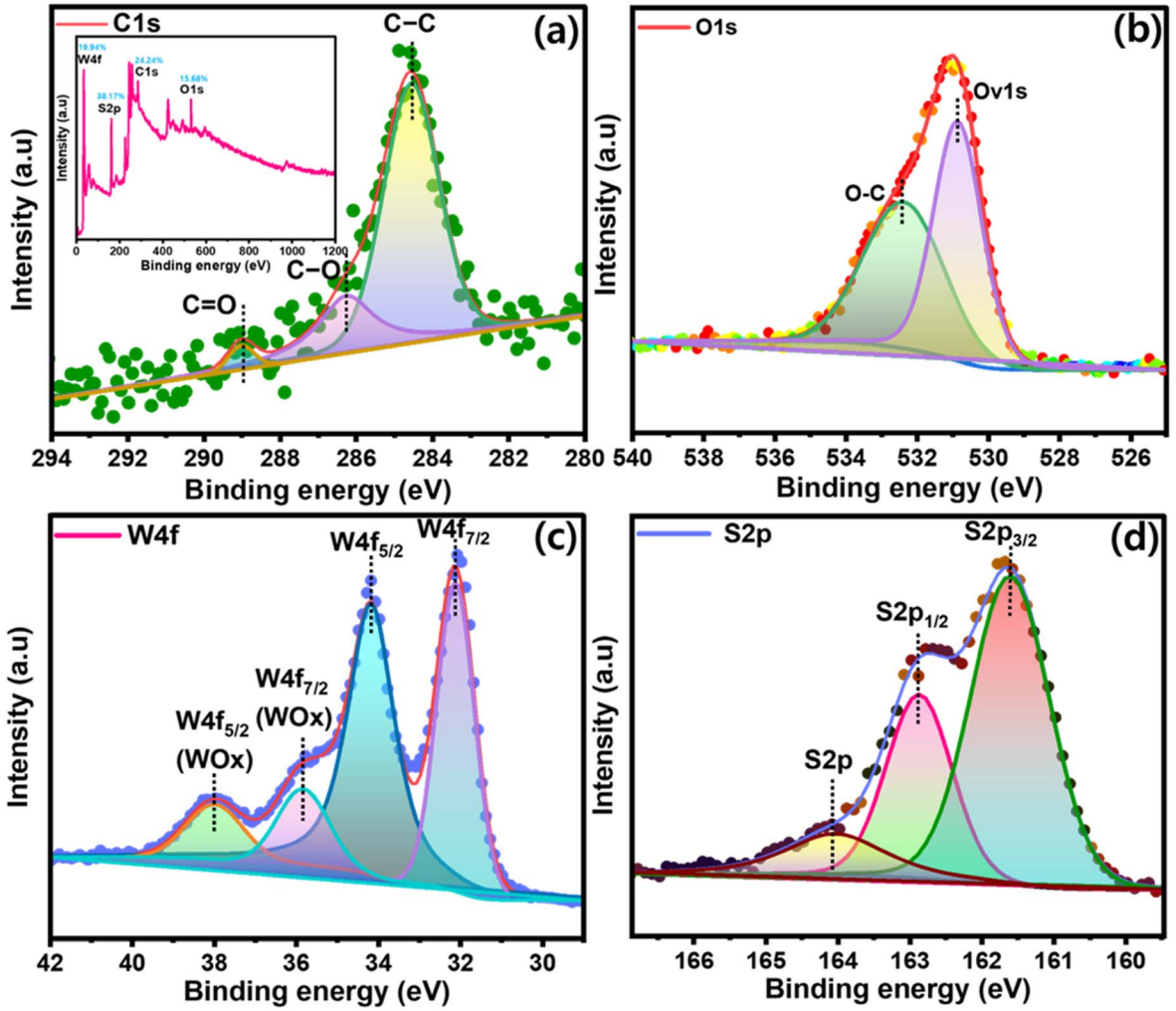

Fig. 5 XPS survey spectra of the sulfur-rich WS_2/rGO composite: (inset of a) full scan survey spectrum, (a) C 1s, (b) O 1s, (c) W 4f, and (d) S 2p.

binding energies of the peaks at 161.86, 163.13 eV, and 164.29 eV denote divalent sulfide ions with S $2p_{3/2}$, S $2p_{1/2}$, and S 2p orbitals, respectively, used for W–S bonding. Fig. 5d shows the existence of unsaturated sulfur, a possible site for humidity (RH) interaction. The two fundamental S $2p_{1/2}$ and S $2p_{3/2}$ peaks represent the common orbital states of S electrons. S has a valence of −2 in WS_2 and is represented by a pair of S $2p_{1/2}$ and S $2p_{3/2}$ peaks. Because of the possibility of the existence of sulfonated species (–SO_3H, the valence of S is +4) in the sulfur-rich WS_2/rGO heterojunction, acid centers may be inhibited. Thus, the peak of the acid centers (SO_4^{2-}, the valence of S is +6) is absent in Fig. 5d. A certain rise may be seen in the area ratio between S$2p_{1/2}$ and S$2p_{3/2}$, indicating an increase in S^{4+} content. The +4 valence of the S element indicates the existence of sulfonated species, –SO_3H, and the sulfur richness of the composite material.[60,83] Furthermore, XPS analysis was performed for all four different compositions to evaluate the content ratio of all the samples (Fig. S7†). WS_2/rGO 20% was found to be the most suitable composite, whereby the XPS data supported the sensing performance, while the overall survey spectrum showed the perfect distribution of all elements together with the highest W and S contents.

3.2. Gas-sensing properties

At RT, the resistive responses of different compositions of sulfur-rich WS_2 and sulfur-rich WS_2/rGO Schottky diode sensors were measured against time at a constant bias of 0.5 V and 10 mA for composition optimization. Three different amounts of oxalic acid (1.11, 2.2, and 3.26 wt%) were used to synthesize sulfur-rich WS_2. The best-performing composition was then used to synthesize a sulfur-rich WS_2/rGO composite containing four different wt% of GO (10%, 20%, 30%, and 40%, respectively) (Table S2†). It was found that the sample with 3.26 wt% oxalic acid in the sulfur-rich WS_2 performed best at RT with a high response value (change in resistance = 220 Ω) (Fig. 6a), which shows it had a high number of acid centers and sulfur richness, which played a key role in improving the sensing response, and so this composition was used to synthesize the sulfur-rich WS_2/rGO composites. A linear trend with an R^2 value of 0.99717 was observed for the response values of the three sulfur-rich WS_2 samples with different oxalic acid contents (Fig. S4c†). Further investigation was done to understand the morphological structure, molecular phase, and oxidation state of the WS_2 nanomaterials with different oxalic acid contents to

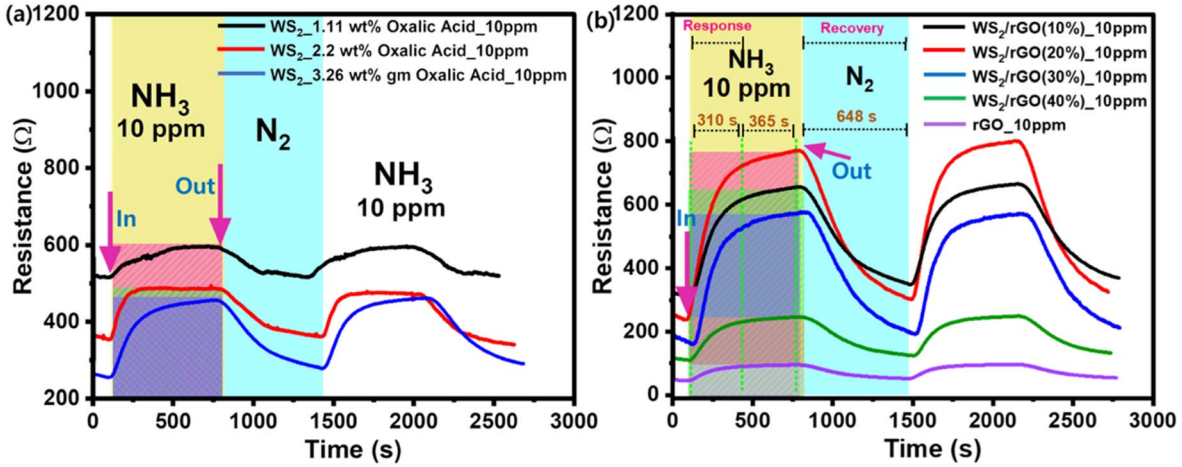

Fig. 6 Composition optimization: (a and b) chemiresistive response optimization of sulfur-rich WS_2 and sulfur-rich WS_2/rGO to 10 ppm NH_3.

study the oxalic acid effect. HRSEM proved that a high oxalic content helped in the uniform formation of WS_2 with homogenous nanoflake decoration over rGO particles. XPS analysis showed that in the presence of a high oxalic content, the W–O-related peaks were minimized in comparison to the low-oxalic-content WS_2, which proved the pure phase for WS_2 formation with fewer WO_x impurity states. Also, as per the at% content of all the elements, the presence of O was the least (facilitating sulfur richness), and W and S were the highest (Table S3†). Furthermore, oxalic acid also reduced the resistance of the WS_2 nanomaterial, which again proved the presence of sulfur richness (Fig. S13†). The trigonal prismatic structure of the WS_2 base plane was composed of a hexagonal sulfur lattice with alternating W atoms. Sulfur-rich WS_2 to rGO heterojunctions enabled the formation of more sulfur-rich WS_2 edge sites because of the increased surface area. Moreover, sulfate (SO_4) groups have been suggested to function as acid centers, which would facilitate the adsorption of NH_3. Resistance was increased by trace sulfonic acid groups (S–O_3H) in sulfur-rich WS_2/rGO because they were more active at adsorbing and taking up electrons from NH_3, which they then transmit to sulfur-rich WS_2 conduction bands. This resistance hampers p-type conductance positive charge flow and generates the high resistive behavior of the sensing material. With increasing the rGO loading density, the resistance of the composite samples decreased due to the conductive nature of the rGO in the composite surface (Fig. S4b and d†). Sulfur-rich WS_2/rGO composite with a 20% rGO content and a 3.26 wt% oxalic acid content performed best and had a higher response value (change in resistance = 525 Ω) at 10 ppm NH_3 than the pristine sulfur-rich WS_2 nanoflakes (Fig. 6b, S4b and d†), and was thus considered the optimum sample. In the presence of rGO, the response value was enhanced due to the increase in surface area, which was directly proportional to the number of accessible active sites (acidic sulfur centers and –OH and OH^- functionalities). The final sulfur-rich WS_2/rGO active sensing nanomaterial was used to study the analytical performance (working voltage, temperature, dynamic response, interference evaluation, stability evaluation, real-time analysis) of the synthesized sulfur-rich WS_2/rGO active material.

Voltage optimization was completed by comparing the sensing responses of our sulfur-rich WS_2/rGO active material at five different voltage magnitudes, *i.e.*, 0.5, 1.0, 1.5, 2.0, and 2.5 V. The sensor resistance was inversely proportional to the applied bias voltage. Upon exposure to NH_3, two clear trends were observed, namely that the sensitivity (response %) and response time (t90) decreased with the bias voltage. The sensor response (%) and t90 are depicted in Fig. S1† as functions of the optimized bias voltage (0.5 V). The sensing response at 0.5 V was better in terms of response and recovery compared to at 1, 1.5, 2, or 2.5 V. Upon applying high voltage, the movement of electrons inside the material from the valence band to the conduction band increased and there was greater positive charge in the conduction band, so due to the entry of electrons in the conduction band, the electrons held positive charge and hampered the flow rate, which led to the increase in resistance at high voltage. In this situation when NH_3 interacts with the surface, it would donate more electrons, which would lead to a decrease in resistance of the material. For a mechanism point of view explanation, refer to Fig. S1.† Furthermore, an *I–V* graph was plotted to confirm the resistance change of the material in the presence of and absence of NH_3 (Fig. S2†). Also, a 0.5 V operating voltage allowed our wireless device to be operated using a coin cell.

A wide range of temperatures ranging from 50 °C to 5 °C were considered to optimize the performance of the sulfur-rich WS_2/rGO composite sensor (Fig. S3†). All the temperatures were controlled by using a thermocontroller (−40 °C to 120 °C) and a chiller setup was used to maintain the temperature at −5 °C, which was connected to the water circulation pathway in the sensing chamber, under the probe station. The response at 5 °C was highest, as was the recovery rate (Fig. S3e†). Upon reducing the temperature sensing response, recovery with a good linearity ($R^2 = 0.99891$) was observed (Fig. S3f†). At 50 °C, the sensor had a response of 25.9% (Fig. S3a†) and this response % value was enhanced by 20% at 30 °C (response % = 45.5%)

(Fig. S3b†), 30% at 20 °C (response % = 55.2%) (Fig. S3c†), 41% at 10 °C (response % = 66%) (Fig. S3d†), and 48% at 5 °C (response % = 72%) (Fig. S3e†). For a mechanism point of view explanation, refer to Fig. S8.† At low temperature, the movement of electrons inside the material from the valence band to the conduction band was the least and the positive charge was greater in the conduction band, which was responsible for the low resistivity, which supports the flow of positive charge. In this situation, when NH_3 interacts with the surface it donates more electrons, which leads to an increase in the resistance of the material. So, at low temperature, more positive charge is available, and at high temperature, less positive charge is available to interact with NH_3, which leads to the inverse trend to the sensing response. Here, 30 °C was set as the operating temperature for the subsequent experiments because our goal was to monitor meat freshness at room temperature.

The response of the sensor increased with the NH_3 concentration. The sensor was exposed to NH_3 concentrations ranging from 2–100 ppm at 70% RH (Fig. 7a). To establish a baseline resistance for saturation purposes, the sensor was exposed to high-purity N_2 (99.99%) before and after gas pulses. When exposed to NH_3, the resistance of the sulfur-rich WS_2/rGO composite gas sensor increased rapidly. The sensor resistance returned to the baseline when the N_2 molecules had been absorbed by the sulfur-rich WS_2/rGO composite after the chamber had been purged with high-purity N_2. The as-prepared device had a huge baseline saturation of 13 Ω min^{-1}. At a relative RH of 45%, the baseline saturation improved to 2 Ω min^{-1} over 9 h. The response and recovery rates also improved; t90 at 10 ppm NH_3 was ~10 min at 70% RH, whereas the recovery period was 20 min at 45% RH. The longer recovery time was probably due to the slower desorption rates of the reaction products from the surface due to the multi-layered structure of the WS_2/rGO composite. Lowering the temperature of the sensor would likely increase the adsorption and desorption rates and accelerate recovery (Fig. S3†). The sensor proved to be capable of detecting different concentrations within the tested concentration range (2–100 ppm) and had higher responses at higher NH_3 concentrations (R^2 = 0.99975).

Operating the sulfur-rich WS_2/rGO composite sensor at 80 °C removed surface impurities and accelerated recovery by increasing the desorption rates. Within the studied NH_3 concentration range (2–100 ppm), the responsiveness of the sensor varied between 18% and 120% (R^2 = 0.99975) (Fig. 7b), which was 3.7 times that of the sulfur-rich WS_2 pristine active material sensor (Fig. 7a) at 30 °C. To determine the LOD of the composite sensor, dynamic sensing analysis was performed at different NH_3 vapor concentrations (0.5–10 ppb and 0.05–1 ppm) (Fig. 7c and d). Compared to the pristine material, the composite material was 10 times more highly sensitive with an LOD value of 0.5 ppb; on the other hand, the pristine material was sensitive only up to 5 ppb. The results showed that the sensor was highly

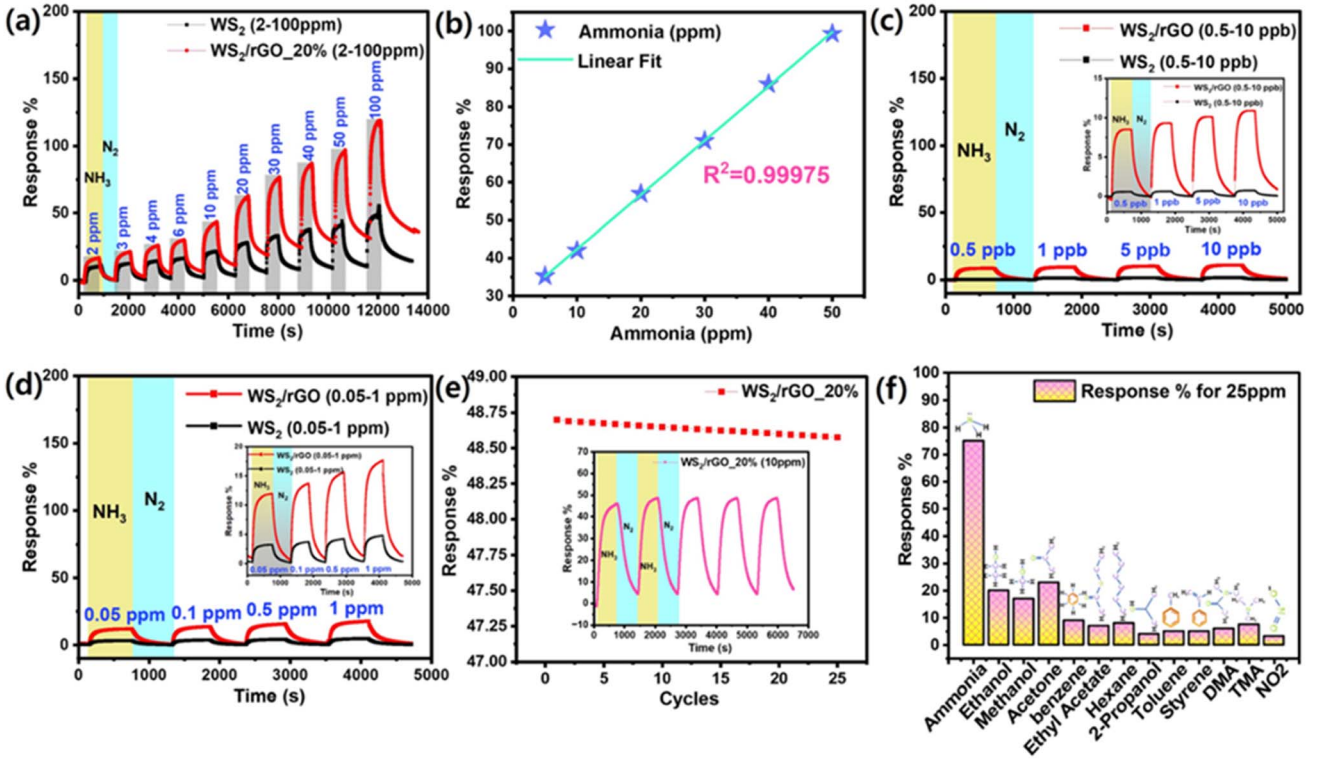

Fig. 7 Dynamic sensing response: (a) comparison of the dynamic sensing responses of sulfur-rich WS_2 and the sulfur-rich WS_2/rGO composite at different NH_3 concentrations (100 ppb to 2 ppm); (b) a linear fitting curve for the sensing response % *versus* NH_3 concentration; (c) LOD up to 0.5 ppb WS_2/rGO composite; (d) dynamic sensing response of the WS_2 and WS_2/rGO composite at different NH_3 vapor concentrations (0.05–1 ppm); (e) repeat sensing cycles of the composite sensor in 10 ppm of NH_3; (f) cross-reactivity sensing response of the composite sensor for different vapors at 25 ppm generated from corresponding aqueous solutions.

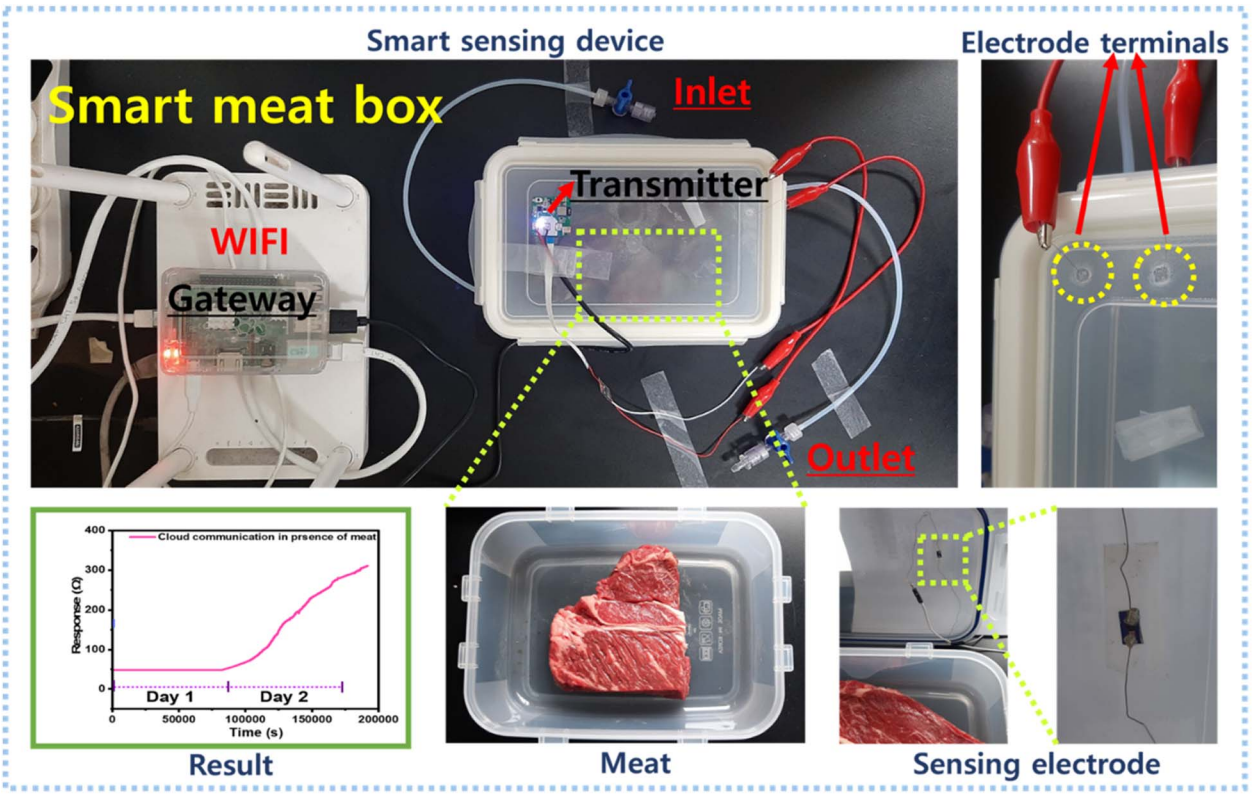

Fig. 8 Schematic representation of the real-time meat spoilage monitoring setup.

stable, with a 97% retention rate up to 25 cycles (Fig. 7e), and could detect ammonia at low levels with an LOD of 0.5 ppb (Fig. 7c). The calculation for the detection limit was based on the standard deviation of the response (Sy) of the curve and the slope of the calibration curve (S) at levels approximating the LOD according to the formula: LOD = 3.3(Sy/S).

The selectivity of the sulfur-rich WS_2/rGO composite sensor for NH_3 in the presence of various VOCs at room temperature is shown in Fig. 7f. At room temperature, the sulfur-rich WS_2/rGO composite sensor responded strongly to 25 ppm NH_3, whereas it had sensitivities of 25–5% for other gases, which had little effect on its selectivity for NH_3. To investigate the long-term stability, composite sensors were aged naturally for a year at ambient temperature. Fig. 7e shows that the response values of aged sulfur-rich WS_2/rGO-based sensors to 10 ppm NH_3 were unchanged even after one year storage at room temperature.

A BLE-based smart meat distribution box was used to monitor meat freshness in real-time (Fig. 8). This system was connected to a computer and a Raspberry Pi, and the IoT and the cloud were used to collect and upload real-time data. A transmitter was coupled to send data to the gateway. A smart IoT gateway was included to process, store, and send data to the cloud infrastructure. The gateway collected information from a local web server and used a website to display information on a screen. The technology could alert individuals by sending notifications to smartphones if an emergency situation arises. Sulfur-rich WS_2/rGO was dropped onto a parallel electrode before being integrated into the BLE device inside the meat distribution box containing fresh meat. Initially, we calibrated and compared the sensing responses of the Keithley setup and the BLE device. The BLE device was coupled to the Keithley sensing chamber, and electrode terminals were used to contact the BLE device. A mass flow controller (MFC) was used to generate NH_3 concentrations of 2–100 ppm to calibrate the BLE device.

The overall sensing performance for the 2–100 ppm NH_3 concentration range was identical for both sensing setups. However, the sensing response was 25% lower for the BLE device, although it did demonstrate good sensitivity, recovery, reproducibility, and linearity (Fig. 9a and b). The freshness levels of meat in real-time were monitored on a daily basis using our cloud communication device (Fig. 8c and d). The meat began to spoil on day two, and the magnitude of the resistance signal increased in direct proportion to the degree of meat spoilage (Fig. 9d). Because a decrease in current is directly proportional to an increase in resistance, the sensing response began to increase as the meat began to spoil and as ammonia was released (Fig. 9d). On day one, the as-prepared device had a massive baseline saturation of 13 Ω min^{-1} at 70% RH (Fig. 9c). On day two, the sensing signal (resistance) increased from 48 to 314 Ω (517% response) (Fig. 9d). An increase in resistance magnitude was observed every 2 h as a result of the NH_3 production. After one and half days, a NH_3 concentration of 150 ppm was reached, indicating the meat was unsuitable for consumption; note, 150 ppm is considered the maximum acceptable value (Fig. S5 and Table S1†). Furthermore, the wireless sensing module was tested in the presence of different gases and their interference was checked with the developed sensor (Fig. S11a, b and Video S1†). Table 1 compares the sensor

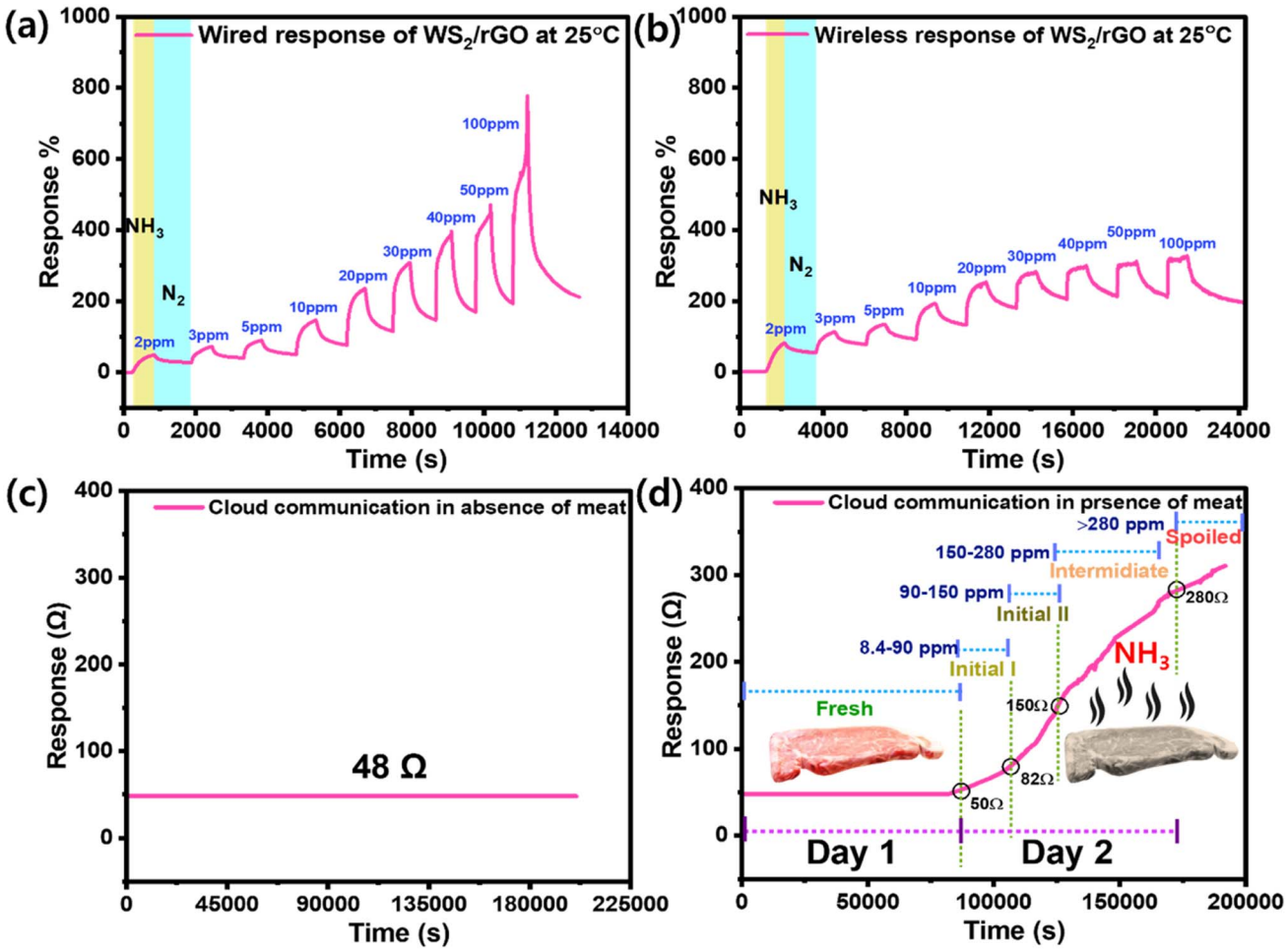

Fig. 9 Calibration of the BLE device: comparison of the dynamic sensing responses of the sulfur-rich WS_2/rGO composite with the Keithley sensing setup (a) and the BLE device (b); (c) and (d) real-time gas-sensing responses *via* the cloud communication system in the absence and presence of meat.

Table 1 Comparison of the sensing performances of our sulfur-rich WS_2/rGO composite and those of other sensors described in the literature

Active materials	Gas concentration (ppm)	Response	Response time and recovery time (s)	Operating temperature	Ref.
rGO	1 ppb	37%	500/long	RT	84
$WS_2/W_{18}O_{49}$	5	25%	73/189	RT	83
WS_2 nanoflakes	10	900%	600/long	RT	85
WS_2	10	3.4	252/648	40 °C (UV light)	62
$W_{18}O_{49}$	1			RT	86
S-rGO/WS_2	10	250%	60/300	28 °C	60
$WO_3/W_{18}O_{49}$	500	23%	13/49	250 °C	87
TiO_2QD/WS_2	250	43%	200/174	RT	88
WS_2/WO_3	10	400%	~150/~100	150 °C	61
Sulfur-rich WS_2/rGO	0.5 (ppb)	18%	310/648	30 °C	This work

performance of our sulfur-rich WS_2/rGO NH_3 sensor with some other sensors in the literature.

3.3. Underlying sensing mechanism

When exposed to reducing gases (NH_3, ethanol, methanol, acetone, benzene, ethyl acetate, hexane, 2-propanol, toluene, and styrene), the resistance of the sulfur-rich WS_2/rGO composite sensor increased, suggesting a p-type behavior, which concurs with previous reports.[89] TEM images of the sulfur-rich WS_2/rGO sensor showed that the rGO (p-type) was covered by a thin layer of sulfur-rich WS_2 (p-type), indicating the creation of p–p junctions and an improved sensing response. Furthermore, upon performing Mott–Schottky (M–S) analysis for WS_2 and WS_2/rGO (Fig. S12†), the WS_2 and WS_2/rGO

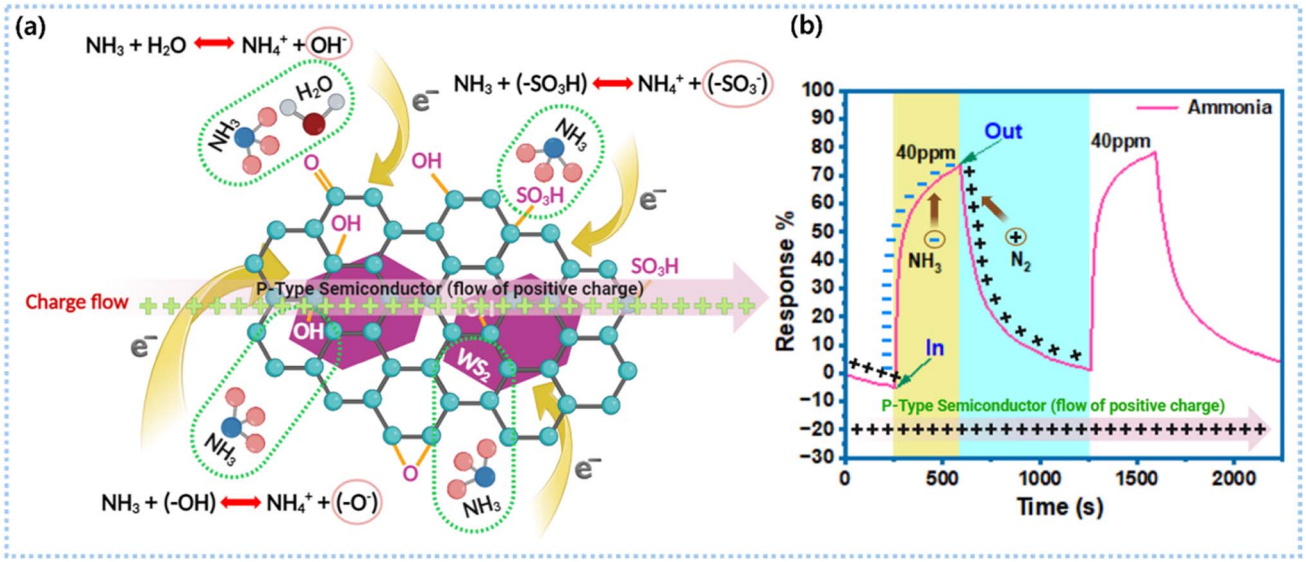

Fig. 10 Sensing mechanism: (a) ammonia sensing mechanism of the sulfur-rich WS_2/rGO nanocomposite and (b) its ammonia sensing response.

electrodes showed negative slopes, indicating the p-type conductivity of the semiconductor.[60,70] The sulfur richness and nitrogen environment play a crucial role in making WS_2 and rGO p-type semiconductors, as S and N act as acceptors and support (enhance) the interaction with NH_3 electrons.[90–92] The sensor exhibited selectivity for NH_3, numerous electric charge-transfer networks supported by the molecular structure of the analyte, analyte–site interactions, and absorption dynamics (physisorption and chemisorption), which could all presumably improve the NH_3 sensing efficiency of the composite sulfur-rich WS_2/rGO sensor (Fig. 10). Hydrogen bonds are formed when the N atom of NH_3 interacts with the hydroxyl H on the surface of rGO, while the channels of hydrogen bonds on graphene facilitate electron transfer from NH_3 to graphene and increase the ohmic resistance.[60,61]

In sulfur-rich WS_2, W is located in the middle layer and is surrounded by S atoms. Furthermore, the high electron density of d-orbitals and the presence of many dangling bonds at sulfur-rich WS_2 edge sites expose highly reactive W atoms and facilitate analyte interactions. Therefore, due to their greater catalytic activity, the exposed edge sites can interact potently with analyte gases. Further, the base plane of sulfur-rich WS_2 has a trigonal prismatic structure with a hexagonal sulfur lattice and alternating W atoms. TEM showed that because sulfur-rich WS_2 was grafted over rGO, it exposed additional sulfur-rich WS_2 edge sites. In addition, sulfate (SO_4) groups have been proposed to act as acid centers at sulfur-rich WS_2/rGO heterojunctions and promote the adsorption of reducing gases. In addition, trace sulfonic acid groups (SO_3H) in sulfur-rich WS_2/rGO can actively accept a greater number of electrons from NH_3 and transfer these to sulfur-rich WS_2 conduction bands, which increases the ohmic resistance (eqn (6) and Fig. 10a).[60,61]

$$NH_3 + (–SO_3H) = NH_4^+ + (–SO_3^-) \quad (6)$$

Further, RH in the sensing environment interacts with the sensor surface while the sensor is exposed to NH_3. Upon exposure to NH_3 vapor, water molecules interact with the sensor surface and are adsorbed as OH^- and $–O^-$ at, for example, surface defects, sulfur vacancies, and unsaturated sulfur. The XPS results confirmed the existence of unsaturated sulfur (Fig. 5d). Hydroxyl ions trap electrons from the conductance band of sulfur-rich WS_2 and thus enhance resistance (Fig. 10a). Simultaneously, NH_3 interacts with the sensor surface and traps more electrons from the conduction band of sulfur-rich WS_2 (eqn (8)), thereby further increasing the sensor resistance.[83]

$$NH_3 + H_2O = NH_4^+ + OH^- \quad (7)$$

$$NH_3 + (–OH) = NH_4^+ + (–O^-) \quad (8)$$

As a result, the NH_3 response of sulfur-rich WS_2/rGO heterojunctions is the direct consequence of multi-charge exchange channel activity.

4. Conclusion

In conclusion, we created a straightforward, highly sensitive, wireless, sulfur-rich WS_2/rGO, NH_3 gas sensor operating at RT for real-time beef freshness monitoring with the following advantages: (a) high ammonia sensitivity, *e.g.*, 46% sensitivity to 10 ppm NH_3 and an LOD of 0.5 ppb, with appropriate signal swapping for BLE devices, (b) allows a BLE device connected to the cloud to be read wirelessly on screen; and (c) allows a simple sensing material synthesis approach using a one-pot hydrothermal reaction and a material compatible with drop-casting, enabling large-scale electrode manufacture. The synergetic strategy of a high acid environment and sulfur richness was used for fabricating a high-performance gas sensor. The enhanced sensing mechanism of sulfur-rich WS_2/rGO could be

explained by the experimental results. Screen-readable beef freshness monitoring was performed using a customized cloud-communicating smart meat distribution box coupled with a BLE device, which demonstrated that the sensing device has potential in the domain of intelligent cloud-communicating monitoring and sensing for many applications, including food safety monitoring and workplace, manufacturing, and health care center monitoring.

Conflicts of interest

The authors declare that they have no known competing financial interests or personal relationships that could have influenced the work reported in this paper.

Acknowledgements

This work was carried out with the support of the "Cooperative Research Program for Agriculture Science and Technology Development (Project No. PJ017067022022)" Rural Development Administration, Republic of Korea.

References

1 X. Xiao, B. Mu, G. Cao, Y. Yang and M. Wang, *J. Sci.: Adv. Mater. Devices*, 2022, **7**, 100430.
2 J. Y. Wu and H. I. Hsiao, *Food Control*, 2021, **120**, 107501.
3 X. Xiao, *Clean. Eng. Technol.*, 2021, **4**, 100148.
4 X. Wang, H. Feng, T. Chen, S. Zhao, J. Zhang and X. Zhang, *Trends Food Sci. Technol.*, 2021, **110**, 483–492.
5 N. Yamazoe, *Sens. Actuators, B*, 2005, **108**, 2–14.
6 X. Xiao, Q. He, Z. Li, A. O. Antoce and X. Zhang, *Food Control*, 2017, **73**, 1556–1563.
7 L. Y. Chang, M. Y. Chuang, H. W. Zan, H. F. Meng, C. J. Lu, P. H. Yeh and J. N. Chen, *ACS Sens.*, 2017, **2**, 531–539.
8 M. M. Swe, T. Eamsa-Ard, T. Srikhirin and T. Kerdcharoen,*2019 IEEE International Conference on Consumer Electronics – Asia, ICCE-Asia 2019*, 2019, pp. 100–103.
9 W. Sun, Y. Liu, L. Jia, M. D. A. Saldaña, T. Dong, Y. Jin and W. Sun, *Int. J. Food Sci. Technol.*, 2021, **56**, 342–351.
10 R. S. Andre, L. A. Mercante, M. H. M. Facure, R. C. Sanfelice, L. Fugikawa-Santos, T. M. Swager and D. S. Correa, *ACS Sens.*, 2022, **7**, 2104–2131.
11 S. Matindoust, G. Farzi, M. B. Nejad and M. H. Shahrokhabadi, *React. Funct. Polym.*, 2021, **165**, 104962.
12 L. Qi, M. Xu, Z. Fu, T. Mira and X. Zhang, *Food Control*, 2014, **38**, 19–29.
13 H. Tabata, Y. Sato, K. Oi, O. Kubo and M. Katayama, *ACS Appl. Mater. Interfaces*, 2018, **10**, 38387–38393.
14 Z. L. Li, X. H. Yi, R. Liu, J. J. Bi, H. Y. Fu, G. P. Zhang, Y. Z. Song and C. K. Wang, *Sci. Rep.*, 2017, **7**, 1–10.
15 I. E. Rosłoń, R. J. Dolleman, H. Licona, M. Lee, M. Šiškins, H. Lebius, L. Madauß, M. Schleberger, F. Alijani, H. S. J. van der Zant and P. G. Steeneken, *Nat. Commun.*, 2020, **11**, 1–6.
16 K. Suematsu, W. Harano, T. Oyama, Y. Shin, K. Watanabe and K. Shimanoe, *Anal. Chem.*, 2018, **90**, 11219–11223.
17 Y. H. Kim, S. J. Kim, Y. J. Kim, Y. S. Shim, S. Y. Kim, B. H. Hong and H. W. Jang, *ACS Nano*, 2015, **9**, 10453–10460.
18 Y. Kim, K. C. Kwon, S. Kang, C. Kim, T. H. Kim, S. P. Hong, S. Y. Park, J. M. Suh, M. J. Choi, S. Han and H. W. Jang, *ACS Sens.*, 2019, **4**, 2395–2402.
19 H. Tang, Y. Li, R. Sokolovskij, L. Sacco, H. Zheng, H. Ye, H. Yu, X. Fan, H. Tian, T. L. Ren and G. Zhang, *ACS Appl. Mater. Interfaces*, 2019, **11**, 40850–40859.
20 X. Xiao, Z. Li, M. Matetic, M. B. Bakaric and X. Zhang, *J. Clean. Prod.*, 2017, **152**, 77–87.
21 P. Escobedo, M. Bhattacharjee, F. Nikbakhtnasrabadi and R. Dahiya, *IEEE Sens. J.*, 2021, **21**, 26406–26414.
22 J. Kim, P. Gutruf, A. M. Chiarelli, S. Y. Heo, K. Cho, Z. Xie, A. Banks, S. Han, K. I. Jang, J. W. Lee, K. T. Lee, X. Feng, Y. Huang, M. Fabiani, G. Gratton, U. Paik and J. A. Rogers, *Adv. Funct. Mater.*, 2017, **27**, 1–8.
23 X. Xiao, Z. Fu, X. Zhang, J. Cheng and M. Yang, *Comput. Electron. Agric.*, 2019, **163**, 104869.
24 T. Stuart, L. Cai, A. Burton and P. Gutruf, *Biosens. Bioelectron.*, 2021, **178**, 113007.
25 C. M. Ou and J. F. Tu, *Microsyst. Technol.*, 2018, **24**, 3977–3983.
26 X. Xiao, Q. He, Z. Fu, M. Xu and X. Zhang, *Food Control*, 2016, **60**, 656–666.
27 H. Feng, J. Chen, W. Zhou, V. Rungsardthong and X. Zhang, *Food Control*, 2019, **98**, 348–358.
28 Y. Tang, Y. Zhao and H. Liu, *ACS Sens.*, 2022, **7**, 3582–3597.
29 J. Zhang, L. Liu, Y. Yang, Q. Huang, D. Li and D. Zeng, *Phys. Chem. Chem. Phys.*, 2021, **23**, 15420–15439.
30 S. Wang, D. Huang, S. Xu, W. Jiang, T. Wang, J. Hu, N. Hu, Y. Su, Y. Zhang and Z. Yang, *Phys. Chem. Chem. Phys.*, 2017, **19**, 19043–19049.
31 Z. Li, H. Li, Z. Wu, M. Wang, J. Luo, H. Torun, P. Hu, C. Yang, M. Grundmann, X. Liu and Y. Fu, *Mater. Horiz.*, 2019, **6**, 470–506.
32 X. Liu, T. Ma, N. Pinna and J. Zhang, *Adv. Funct. Mater.*, 2017, **27**, 1–30.
33 H. J. Kim and J. H. Lee, *Sens. Actuators, B*, 2014, **192**, 607–627.
34 N. Barsan, D. Koziej and U. Weimar, *Sens. Actuators, B*, 2007, **121**, 18–35.
35 G. Korotcenkov and B. K. Cho, *Sens. Actuators, B*, 2017, **244**, 182–210.
36 J. Zhang, Z. Qin, D. Zeng and C. Xie, *Phys. Chem. Chem. Phys.*, 2017, **19**, 6313–6329.
37 A. Dey, *Mater. Sci. Eng., B*, 2018, **229**, 206–217.
38 H. Ji, W. Zeng and Y. Li, *Nanoscale*, 2019, **11**, 22664–22684.
39 N. Yamazoe and K. Shimanoe, *Sens. Actuators, B*, 2008, **128**, 566–573.
40 C. Anichini, W. Czepa, D. Pakulski, A. Aliprandi, A. Ciesielski and P. Samorì, *Chem. Soc. Rev.*, 2018, **47**, 4860–4908.
41 C. Mackin, A. Fasoli, M. Xue, Y. Lin, A. Adebiyi, L. Bozano and T. Palacios, *2d Mater*, 2020, **7**(2), 022002.
42 A. Bag and N. E. Lee, *J. Mater. Chem. C*, 2019, **7**, 13367–13383.
43 R. A. Potyrailo, *Chem. Rev.*, 2016, **116**, 11877–11923.

44 R. Jha, A. Nanda and N. Bhat, *IEEE Sens. J.*, 2021, **21**, 10211–10218.
45 X. Li, Y. Zhao, X. Wang, J. Wang, A. M. Gaskov and S. A. Akbar, *Sens. Actuators, B*, 2016, **230**, 330–336.
46 W. Zhou, J. Han, D. Kong, Y. Gao, Y. Gao, Y. Wang and G. Lu, *Sens. Actuators, B*, 2023, **396**, 134614.
47 Q. Feng, X. Li, J. Wang and A. M. Gaskov, *Sens. Actuators, B*, 2016, **222**, 864–870.
48 Q. Feng, X. Li and J. Wang, *Sens. Actuators, B*, 2017, **243**, 1115–1126.
49 J. Han, D. Kong, W. Zhou, Y. Gao, Y. Gao, G. Liu, F. Liu, C. G. Wang, P. Sun and G. Lu, *Sens. Actuators, B*, 2022, **371**, 132596.
50 M. Rethinasabapathy, G. Bhaskaran, S. K. Hwang, T. Ryu and Y. S. Huh, *Chemosphere*, 2023, **336**, 139256.
51 G. Bhaskaran, M. Rethinasabapathy, J. Shin, K. S. Ranjith, H. U. Lee, W. K. Son, Y. K. Han, T. Ryu and Y. S. Huh, *J. Colloid Interface Sci.*, 2023, **650**, 752–763.
52 J. C. Jiang, J. Liu, Y. Piao, M. S. Zhang and L. Y. Meng, *Carbon Lett.*, 2023, **33**, 89–97.
53 Y. Zhang, J. Huang, Z. Dong, Y. Zhan, J. Xi, J. Xiao, S. Huang and F. Tian, *Carbon Lett.*, 2023, **33**, 77–87.
54 Y. Gao, W. Zhou, D. Kong, J. Han, Y. Gao and G. Lu, *ACS Appl. Nano Mater.*, 2023, **6**, 19588–19599.
55 D. K. Dey, J. I. Kang, V. K. Bajpai, K. Kim, H. Lee, S. Sonwal, J. Simal-Gandara, J. Xiao, S. Ali, Y. S. Huh, Y. K. Han and S. Shukla, *Crit. Rev. Food Sci. Nutr.*, 2023, **63**, 8489–8510.
56 S. Sonwal, S. Shukla, M. Alhammadi, R. Umapathi, H. P. K. Sudhani, Y. Cho and Y. S. Huh, *Mater. Adv.*, 2023, **4**, 4390–4399.
57 V. K. Bajpai, S. Sonwal, S. K. Hwang, S. Shukla, I. Khan, D. K. Dey, L. Chen, J. Simal-Gandara, J. Xiao, Y. S. Huh and Y. K. Han, *Pharmacol. Res.*, 2021, **163**, 107044.
58 M. Alhammadi, J. Yoo, S. Sonwal, S. Y. Park, R. Umapathi, M. H. Oh and Y. S. Huh, *Front. Nutr.*, 2022, **9**, 1036826.
59 J. Jiang, P. Trundle, J. Ren, Y.-L. Cheng, C.-Y. Lee, Y.-L. Huang, C. A. Buckner, R. M. Lafrenie, J. A. Dénommée, J. M. Caswell, D. A. Want, G. G. Gan, Y. C. Leong, P. C. Bee, E. Chin, A. K. H. Teh, S. Picco, L. Villegas, F. Tonelli, M. Merlo, J. Rigau, D. Diaz, M. Masuelli, S. Korrapati, P. Kurra, S. Puttugunta, S. Picco, L. Villegas, F. Tonelli, M. Merlo, J. Rigau, D. Diaz, M. Masuelli, M. Tascilar, F. A. de Jong, J. Verweij, R. H. J. Mathijssen, J. Amin, M. Sharif, N. Gul, S. Kadry, C. Chakraborty, V. Dutt, S. Chandrasekaran and V. García-Díaz, in *Meat and Nutrision*, Intech open, 2010, vol. 34, pp. 57–67.
60 X. Wang, B. Huang, X. Wu, D. Gu and X. Li, *Sens. Actuators, B*, 2021, **337**, 129776.
61 X. Li, X. Li, Z. Li, J. Wang and J. Zhang, *Sens. Actuators, B*, 2017, **240**, 273–277.
62 D. Gu, X. Li, H. Wang, M. Li, Y. Xi, Y. Chen, J. Wang, M. N. Rumyntseva and A. M. Gaskov, *Sens. Actuators, B*, 2018, **256**, 992–1000.
63 N. Huo, S. Yang, Z. Wei, S. S. Li, J. B. Xia and J. Li, *Sci. Rep.*, 2014, **4**, 1–9.
64 S. Sardana and A. Mahajan, *ACS Appl. Nano Mater.*, 2023, **6**, 469–481.
65 S. Sardana, H. Kaur, B. Arora, D. K. Aswal and A. Mahajan, *ACS Sens.*, 2022, **7**, 312–321.
66 S. Sardana, A. K. Debnath, D. K. Aswal and A. Mahajan, *Sens. Actuators, B*, 2023, **394**, 134352.
67 R. Umapathi, B. Park, S. Sonwal, G. M. Rani, Y. Cho and Y. S. Huh, *Trends Food Sci. Technol.*, 2022, **119**, 69–89.
68 R. Umapathi, S. M. Ghoreishian, S. Sonwal, G. M. Rani and Y. S. Huh, *Coord. Chem. Rev.*, 2022, **453**, 214305.
69 R. Umapathi, S. Sonwal, M. J. Lee, G. Mohana Rani, E. S. Lee, T. J. Jeon, S. M. Kang, M. H. Oh and Y. S. Huh, *Coord. Chem. Rev.*, 2021, **446**, 214061.
70 R. Xie, J. Lu and J. Wang, *J. Ind. Eng. Chem.*, 2024, **131**, 248–256.
71 D. Y. Nadargi, A. Umar, J. D. Nadargi, S. A. Lokare, S. Akbar, I. S. Mulla, S. S. Suryavanshi, N. L. Bhandari and M. G. Chaskar, *J. Mater. Sci.*, 2023, **58**, 559–582.
72 Z. Yin, Y. Yang, C. Hu, J. Li, B. Qin and X. Yang, *NPG Asia Mater.*, 2022, **16**(8), 2024.
73 X. Liu, X. Zhou, C. Yang, W. Yang, G. Liu, Y. Li, G. Zhang and X. Zhao, *J. Ind. Eng. Chem.*, 2023, **124**, 323–330.
74 J. Yang, Q. Kang, B. Zhang, X. Tian, S. Liu, G. Qin and Q. Chen, *J. Ind. Eng. Chem.*, 2022, **115**, 162–170.
75 S. G. Kim, T. V. Tran and J. S. Lee, *J. Ind. Eng. Chem.*, 2022, **112**, 423–429.
76 S. Rasheed, N. Ahmad, M. Anwar ul Haq, W. Ahmad, D. Hussain and Sirajuddin, *J. Ind. Eng. Chem.*, 2023, **128**, 450–458.
77 A. Neog and R. Biswas, *Mater. Res. Bull.*, 2021, **144**, 111471.
78 C. S. Rout, P. D. Joshi, R. V. Kashid, D. S. Joag, M. A. More, A. J. Simbeck, M. Washington, S. K. Nayak and D. J. Late, *Sci. Rep.*, 2013, **3**, 1–8.
79 X. Zhang, H. Xu, J. Wang, X. Ye, W. Lei, M. Xue, H. Tang and C. Li, *Nanoscale Res. Lett.*, 2016, **11**, 442.
80 M. Latha and J. Vatsala Rani, *J. Electrochem. Soc.*, 2020, **167**, 070501.
81 F. T. Johra and W. G. Jung, *Appl. Surf. Sci.*, 2015, **357**, 1911–1914.
82 G. Chen, X. Hu, M. Gu, H. Wu, K. Chen, H. Yu, B. Ren, Z. Li, Y. Luan, T. Tang, Y. Cheng, H. Huang, L. Chen, B. Y. Zhang and J. Z. Ou, *Adv. Funct. Mater.*, 2022, **32**(41), 2202239.
83 M. Manoharan, K. Govindharaj, K. Muthumalai, R. Pandian, Y. Haldorai and R. T. Rajendra Kumar, *ACS Appl. Mater. Interfaces*, 2023, **15**, 4703–4712.
84 F. Schedin, A. K. Geim, S. V. Morozov, E. W. Hill, P. Blake, M. I. Katsnelson and K. S. Novoselov, *Nat. Mater.*, 2007, **6**, 652–655.
85 F. Perrozzi, S. M. Emamjomeh, V. Paolucci, G. Taglieri, L. Ottaviano and C. Cantalini, *Sens. Actuators, B*, 2017, **243**, 812–822.
86 Y. M. Zhao and Y. Q. Zhu, *Sens. Actuators, B*, 2009, **137**, 27–31.
87 Y. Xiong, Z. Zhu, T. Guo, H. Li and Q. Xue, *J. Hazard. Mater.*, 2018, **353**, 290–299.
88 Z. Qin, C. Ouyang, J. Zhang, L. Wan, S. Wang, C. Xie and D. Zeng, *Sens. Actuators, B*, 2017, **253**, 1034–1042.

89 X. Wang, B. Huang, X. Wu, D. Gu and X. Li, *Sens. Actuators, B*, 2021, **337**, 129776.
90 Q. Cao, Y.-W. Dai, L. C. Jing Xu, H. Zhu, Q.-Q. Sun and D. W. Zhang, *ACS Appl. Mater. Interfaces*, 2017, **9**, 18215–18221.
91 N. D. K. Tu, J. Choi, C. R. Park and H. Kim, *Chem. Mater.*, 2015, **27**, 7362–7369.
92 H. Seo, S. Ahn, J. Kim, Y. A. Lee, K. H. Chung and K. J. Jeon, *Sci. Rep.*, 2014, **4**, 1–7.